SOUND RADIATION FROM ELLIPTIC VORTEX RINGS: EVOLUTION AND INTERACTION

K.-W. Ryu and D.-J. Lee

Laboratory of Aerodynamics and Aeroacoustics, Department of Aerospace Engineering, Korea Advanced Institute of Science and Technology, 373-1, Kusong-Dong Yusong-Ku, Taejon 305-701, Korea

Sound generation from the evolution and interaction of elliptic vortex rings is calculated numerically. An elliptic vortex ring emits a strong sound signal due to significant distortion and stretching of the vortex filament. At the far field, the acoustic pressure is linearly dependent on the third time derivatives of the vortex positions. Therefore, a numerical scheme of high resolution is employed to describe in detail the elliptic vortex ring motions, which are highly non-linear. Discretized vortex filaments are interpolated by using a parametric blending function to remove a possible numerical instability. The distorted vortex filament, owing to the self-induced velocity and the induced velocity from the other vortex segments, is redistributed at each time step. The accuracy and efficiency of the scheme are validated by comparisons with the analytic solution of circular vortex ring interaction. Acoustic signals from the evolution of a single elliptic vortex ring are obtained with various aspect ratios of the axes. Vortex motions and acoustic signals from two identical elliptic vortex rings, placed initially with selected separation distances, are calculated. Distinct periods are obtained from the evolution of each single elliptic vortex ring and the pairing process of two elliptic vortex rings. The calculated periods in the acoustic signals depend to a significant degree on the initial aspect ratio of the ring and the separation distance.

© 1997 Academic Press Limited

1. INTRODUCTION

Sound generation from unsteady vortical flows has been studied by many researchers [1–5]. One typical vortex flow is the evolution and interaction of vortex rings, which has been recognized as a fundamental flow noise source. The acoustic field can be obtained by using acoustic analogy or by matched asymptotic expansion. It is shown that the sound source term at low Mach number is linearly dependent on the third time derivatives of the vorticity distributions and their position vectors. Therefore, to obtain the sound pressure accurately, detailed descriptions of the vortex motion are required.

The motion of an elliptic vortex ring is three-dimensional and highly non-linear because of the differing curvature along the ring. Hence, it is necessary to develop a numerical method of high resolution, describing the distorted vortex motion in detail. It is obvious that numerical errors in the motion may lead to misinterpretations of calculated acoustic results.

Earlier work about the motion of the elliptic vortex ring was done by Arms and Hama [6]. They used a Local Induction Approximation (LIA), with the assumptions that the core size of the ring is extremely small and that the long distance induction is neglected. Then the filament of the ring is moved only with a local self-induced velocity, proportional to

the local filament curvature. The contributions from the other parts of the vortex filament are neglected. An extensive study about the evolution of the single elliptic vortex ring was undertaken numerically by Dhanak and De Bernardinis [7]. They obtained reasonable results compared with experimental data for various initial aspect ratios (minor to major axes ratios) of elliptic configurations. The cut-off approach developed by Moore and Rosenhead was adopted to remove the singularity problem [8] in the Biot–Savart law in describing the vortex motion. The interesting phenomenon in the motion of an elliptic vortex ring is the "axis switching motion". The translational velocity of the major axis is higher than that of the minor axis because its velocity is inversely proportional to its radius of curvature. As a sequence, both end parts of the major axis move ahead of the initial elliptic vortex ring. After some evolution the major axis is switched to minor axis and vice versa.

The sound from the motion of a single elliptic vortex ring was calculated by Möhring [9]. He used the LIA to obtain the vortex motion and the vector Green function [3] to obtain the final expression from the far field sound pressure. A nearly periodic change of directions of preferential radiation was obtained due to axis switching for a moderate aspect ratio of minor to major axis. However, it lost a periodic tendency below an aspect ratio of 0·6. The patterns of the sound radiation were closely related to the initial shape of the ring. He also calculated a sound field from a system of two elliptic rings with the same methods, to explain the experimental observation of preferential radiation direction for a laminar elliptic jet, done by Bridges and Hussain [10]. According to the experimental results, the acoustic pressure radiated preferentially to the minor axis of the ellipse. Möhring showed numerically that the radiation in the direction of the minor axis dominates for moderate initial separation distances between the two vortex rings. He found that the sound is radiated with a "leap-frogging motion" of the elliptic vortex rings, which is similar to the motion of two circular vortex rings. The leap-frogging motion, as it is sometimes called, is the mutual threading motion in the pairing process where the trailing vortex ring contracts and rushes through the leading vortex that is already enlarged, and this slip-through process is repeated with an exchange of roles.

The pairing phenomena [10] of the leap-frogging motion for the two circular rings can be analytically described by using equations of motion which were derived by Dyson for thin circular vortex rings [11]. The radiated sound pressure from the two vortex rings was obtained by Kambe and Minota [4] by using the analytic formula for the vortex motions. They observed that the acoustic pressure has a peak value in the direction of the convecting motion when the one vortex ring slips through the other during the mutual threading motion. They also observed that the amplitudes of the acoustic pressures are highly dependent on the initial separation distance between the rings. Recently, the noise mechanism from the pairing process in a circular jet was investigated by Tang and Ko [12], both theoretically and experimentally.

A variety of flow and sound patterns are expected for the system of elliptic rings owing to axis switching and the pairing phenomena. Therefore, more accurate motions of the elliptic vortices should be obtained to calculate the sound pressure from the interaction of the elliptic vortex rings of various aspect ratios and initial separation distances.

It is the aim of this paper to develop a stable, accurate and efficient numerical tool for describing the elliptic vortex motions and to calculate the acoustic signals for various initial conditions. Some results of the vortex motions are highly distorted from the given initial conditions, which can be obtained by employing a parametric blending curve function to interpolate the discretized vortex filament at each time step. The equation of filament motion is integrated by using the Gaussian quadrature rule. Several numerical points are inserted along the filaments whenever the filaments are severely distorted after
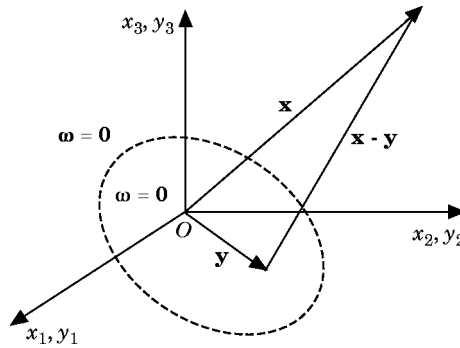
Figure 1. A schematic view of the co-ordinate system.

redistributing the vortex segments. The cut-off theory is adopted in this paper instead of the LIA. The accuracy of the scheme is validated by comparing the analytic solutions of the two circular vortex rings. The efficiency is also checked by comparing the numerical results with those obtained by Dhanak and De Bernardinis [7] for the single elliptic vortex rings. The far field sound pressure are calculated for the single elliptic vortex with various aspect ratios by using the vortex source term obtained by Möhring [3]. The vortex motions and the acoustic pressures are also calculated for the system of two elliptic vortex rings with several initial separation distances and aspect ratios.

2. MATHEMATICAL REPRESENTATIONS

2.1. ACOUSTIC FIELDS

The acoustic field due to flow fluctuations can be described as follows:

$$\frac{1}{a_0^2} \frac{\partial^2 p}{\partial t^2} - \nabla^2 p = q, \tag{1}$$

where p is the acoustic pressure, a_0 is the ambient acoustic velocity, and q is the acoustic source term. At low Mach number, Lighthill [13] proposed the acoustic source term as $q \approx \rho_0 \partial^2 v_i v_j / \partial x_i \, \partial x_j$, where $\mathbf{v}$ is the velocity of an incompressible flow and ρ_0 is the density of the ambient fluid. By using the free space Green function $G(\mathbf{x}, \mathbf{y}, t - \tau)$, the solution of equation (1) in the integral form can be obtained as

$$p(\mathbf{x}, t) = \int G(\mathbf{x}, \mathbf{y}, t - \tau) q(\mathbf{y}, \tau) \, \mathrm{d}^3 \mathbf{y} \, \mathrm{d}\tau, \tag{2}$$

where $\tau = t - |\mathbf{x} - \mathbf{y}|/a_0$ is the retarded time, $\mathbf{x}$ is the observation position vector and $\mathbf{y}$ is the acoustic source position vector, as shown in Figure 1.

Möhring [3] introduced the vector Green function $\mathbf{G}(\mathbf{x}, \mathbf{y}, t - \tau)$, which obeys the relation $\nabla_y G = \nabla_y \times \mathbf{G}$, and obtained the final form of the equation (2) for low Mach number flows in the far field:

$$p(\mathbf{x}, t) = \frac{\rho_0}{12\pi a_0^2 x^3} \frac{\partial^3}{\partial t^3} \int (\mathbf{x} \cdot \mathbf{y}) \mathbf{y} \cdot (\boldsymbol{\omega} \times \mathbf{x}) \, \mathrm{d}^3 \mathbf{y}, \tag{3}$$

where $x = |\mathbf{x}|$ and $\boldsymbol{\omega}$ is the vorticity in the flow field. Equation (3) can be expressed in compact form for the vortex filament:

$$p(\mathbf{x}, t) = \frac{\rho_0}{12\pi a_0^2} \sum_{i,k} \frac{\dddot{Q}_{ik}(t - x/a_0) x_i x_k}{x^3},$$ (4)

with

$$Q_{ik} = \int y_i (\mathbf{y} \times \boldsymbol{\omega})_k \, \mathrm{d}^3\mathbf{y} = \Gamma \int y_i (\mathbf{y} \times \mathrm{d}\mathbf{y})_k,$$ (5)

where Γ denotes a circulation of the vortex filament, and $\mathrm{d}\mathbf{y}$ a curve element in the tangential direction of the vortex filament. $\dddot{Q}_{ik}$ denotes the third time derivative of Q_{ik}. The only non-vanishing components of Q_{ik} are its diagonal elements Q_{11}, Q_{22} and Q_{33}, which additionally satisfy the relation $Q_{11} + Q_{22} + Q_{33} = 0$ of vanishing trace. The tree components of the Q_{ii} are related to the acoustic pressures in the three axis directions respectively.

2.2. FLOW FIELDS

The acoustic field is closely related to the vortex position at each time step, as indicated in equations (4) and (5). The velocity at ξ_0 of a vortex filament with circulation Γ is given by the usual cut-off approach, which was formulated by Moore and Rosenhead (see reference [8]). It is defined as

$$\frac{\partial \mathbf{y}(\xi_0, t)}{\partial t} = \frac{\Gamma}{4\pi} \int_c \frac{\partial \mathbf{y}(\xi, t)}{\partial \xi} \times \frac{\mathbf{y}(\xi_0, t) - \mathbf{y}(\xi, t)}{\{|\mathbf{y}(\xi_0, t) - \mathbf{y}(\xi, t)|^2 + \mu^2(t)\}^{3/2}} \, \mathrm{d}\xi,$$ (6)

where $\mathbf{y}(\xi, t)$ is the position vector of a material point, denoted by Lagrangian variable ξ at time t. The Rosenhead cut-off parameter $\mu(t)$ is used to remove the singularity problem in the Biot–Savart law at $\xi = \xi_0$. The parameter $\mu(t) = 2\delta_R c(t)$ is proportional to the core radius $c(t)$. The coefficient δ_R depends on the vorticity distribution across the core of the vortex filament. We adopt $\delta_R = (1/2)\exp(-A - 1/2)$ with $A = 1$ [7].

As indicated in equation (6), the dynamics of the filament are very dependent on the core size $c(t)$ and the initial configuration of the filament $\mathbf{y}(\xi, t = 0)$. The initial circular core radius c_0 of the elliptic vortex ring at time $t = 0$, proposed by Saffman [14], is adopted here:

$$c_0 = 8\sqrt{ab} \exp\left[-\frac{\pi^2}{2\sqrt{6}} - 1 + A - \left(1 - \frac{e^2}{2}\right) \frac{\mathbf{K}(e)}{\mathbf{E}(e)} \right],$$ (7)

where a and b are the lengths of semi-major and semi-minor axes of the ellipse respectively. $\mathbf{K}(e)$ and $\mathbf{E}(e)$ are the elliptic integral of the first and second kind respectively, and e is the eccentricity of the ellipse; that is, $e^2 = (a^2 - b^2)/a^2$.

The centroid of the vorticity at time t_1 is defined [14] as

$$\mathbf{y}_c(t_1) = \frac{\Gamma}{2} \int \frac{\mathbf{y} \times \mathbf{t} \cdot \mathbf{I}}{|\mathbf{I}|^2} \mathbf{y} \, \mathrm{d}s,$$ (8)
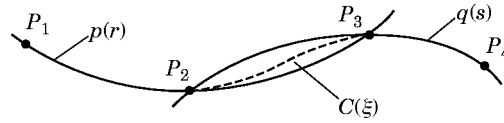
Figure 2. The notation for the parametric blending curve.

where $\mathbf{y}_c = (y_{1c}, y_{2c}, y_{3c})$ and $\mathbf{y} = (y_1, y_2, y_3)$. The symbols $\mathbf{t}$ and s represent the tangential unit vector along the vortex filament and the local distance along the vortex filament respectively. The symbol $\mathbf{I} = \Gamma \oint \mathbf{y} \times \mathbf{t} \, ds$ represents the impulse vector of vortex ring, which is conserved over time. The velocity of the vorticity centroid $\mathbf{U}_c(t_1)$ can be obtained from $d\mathbf{y}_c(t_1)/dt$.

3. INTERPOLATIONS AND VALIDATIONS

3.1. INTERPOLATIONS

There are many mathematical expressions to represent the three-dimensional curves of $\mathbf{y}(\xi, t)$ in equation (6). Generally, cubic spline curves are used to interpolate the curves. However, the spline curves do have certain disadvantages [15]. Among these are the non-intuitive effects of tangential vector direction and difficulties of the end conditions. The interpolation requires inversion of a large tri-diagonal matrix, and a change in any one segment affects all the spline segments. Therefore, the curve is not adequate to represent the vortex filament motion in strong interaction problems because the local disturbed curvature (instability due to the numerical error) of the vortex filaments affects the global motion and the acoustic signal significantly.

The parabolic blending curves, employed here, maintain the continuity of the first derivative in space, which is critical in our problem. The parabolic blending curve, $C(\xi)$, is given by

$$C(\xi) = (1 - \xi)p(r) + \xi q(s), \tag{9}$$

The functions $p(r)$ and $q(s)$ are parametric parabolas through P_1, P_2, P_3 and P_2, P_3, P_4, respectively, as shown in Figure 2. In reference [15], a generalized parametric blending curve is developed from the assumption of normalized chord length approximation for the position parameters, r and s at P_2 and P_3, respectively, which are linearly related to the parameter ξ, i.e., $0 \leqslant r, s, \xi \leqslant 1$. Therefore the functions $p(r)$ and $q(s)$ are cubic equations of the parameter ξ. According to the generalized parabolic blending function, equation (9) may be rewritten in matrix form as

$$C(\xi) = [\xi^3, \xi^2, \xi, 1][A][G], \tag{10}$$

where $[A]$ is a blending function matrix consisting of $p(r)$, $q(s)$ and ξ, and $[G]$ is a geometric matrix that is constructed by the position vector at P_1, P_2, P_3 and P_4. We apply this blending curve to equation (6). The spatial derivatives at an arbitrary position on the curve $C(\xi)$ can easily be obtained as

$$\partial C(\xi)/\partial \xi = [3\xi^2, 2\xi, 1, 0][A][G], \tag{11}$$

The curve information is represented by the mathematical curve equation; that is, parabolic blending curve. We use this interpolation equation to calculate all of the three-dimensional curve integration (equations (5), (6) and (8)) at every time step.
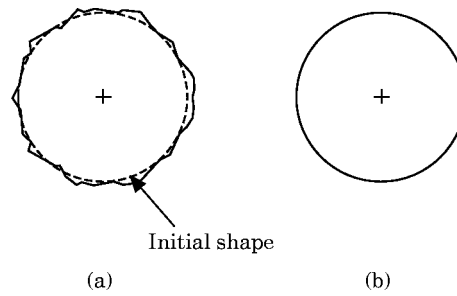
Figure 3. A plane view of the evolution results for the circular vortex ring at $t = 7$, to compare the stability for two types of curves ($\Gamma = 4\pi$, $\Delta t = 0.01$, $b/a = 1$; circular vortex ring). (a) Spline curve; (b) parabolic blending curve.

3.2. DISCRETIZATIONS

The continuous vortex filament is divided into several vortex segments in the integral scheme. To prevent instability due to numerical error, it is efficient to redistribute the numerical points described by the interpolation function on the vortex filament curve. The total length of the filament at each time step is calculated to obtain the core radius of $c(t)$, which is assumed to be constant along the filament but changes at each time step. That is, it can be determined in view of the constant of the cross-section along the filament and the total volume conservation of the filament core, with the assumption of incompressibility of the total core volume in the incompressible flow. In this study, the evolution of the vortex ring can be determined simply by integrating the right side of the equation (6) by using the seven-point Gaussian quadrature rule for curve integration, and the fourth order Runge–Kutta method for time stepping. The three components of the spatial derivatives can easily be obtained by using equation (11) for the position vector $\mathbf{y}(\xi, t)$ instead of $C(\xi)$, as shown in equation (10), the interpolation of which is much more critical to remove the numerical instability.

We limit the maximum number of points to 180 along the loop of each vortex filament. At each time, additional numerical points are inserted if the length of a segment is larger than twice the initial length.
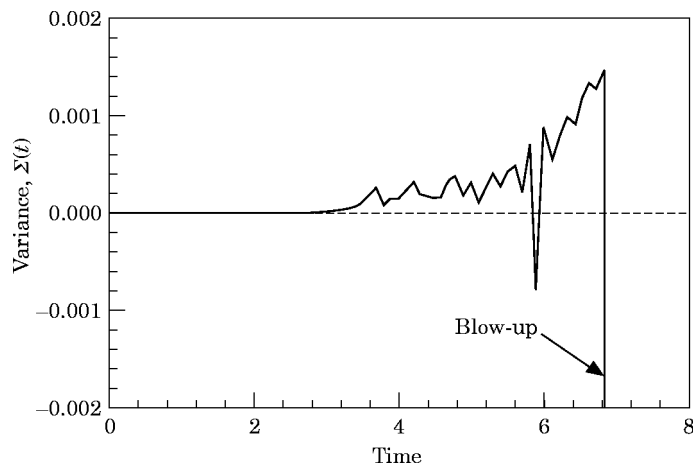

Figure 4. A plot of the variance versus time for the circular vortex ring, to compare the parabolic blending curve (– – – –) with the spline (——) ($\Gamma = 4\pi$, $\Delta t = 0.01$, $c_0 = 0.3925$, $b/a = 1$).
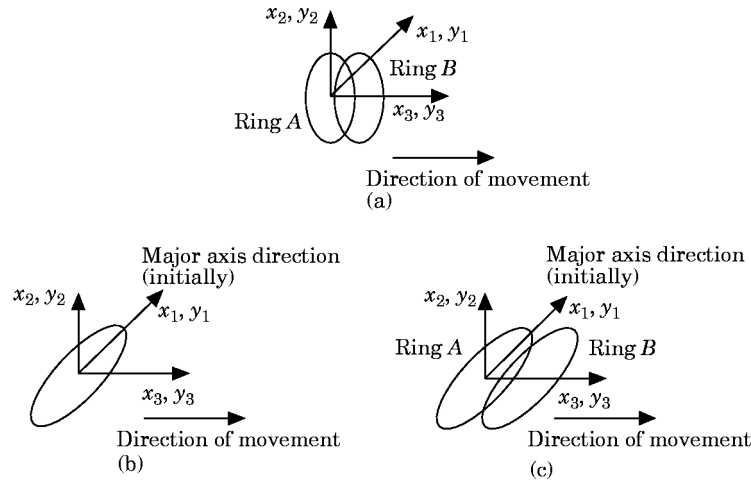
Figure 5. Schematic views of the model problems. (a) Two circular vortex rings; (b) single elliptic vortex ring; (c) two elliptic vortex rings.

3.3. VALIDATIONS

The numerical stabilities of circular vortex ring evolution interpolated by the two different schemes are compared in Figure 3. The same initial conditions ($\Gamma = 4\pi$, $N = 41$, $\Delta t = 0\cdot01$) are used for the circular vortex rings, which are expected to maintain the initial circular shape and move with a constant velocity. In Figure 3(a) spline curves were used and in Figure 3(b) parabolic blending curves were used. The vortex ring with the spline curves is highly distorted at numerical time $t \approx 7$ due to numerical errors. However, the vortex ring with parabolic blending curves maintains the initial circular shape. In Figure 4 is shown the time history of the variance of the two schemes. The variance $\Sigma(t)$ can be represented as

$$\Sigma(t) = \frac{1}{2\pi a^3 b} \oint \left(y_1 \frac{\mathrm{d}y_2}{\mathrm{d}s} - y_2 \frac{\mathrm{d}y_1}{\mathrm{d}s} \right)(y_3 - y_{3c})^2 \, \mathrm{d}s. \tag{12}$$

This represents the deviation of the flatness from the initial filament curves. In Figure 3(a), the result shows the difficulties at the cyclic end condition for the spline curves occurring from the initial stage; and error in any segment affects the final curve shapes. On the other hand, in Figure 3(b) it is indicated that the parabolic blending curve suffers from no such difficulties. It is very stable and efficient for unsteady large time marching problems.

4. RESULTS AND DISCUSSION

We used the above numerical schemes to study three typical model problems as shown in Figure 5. Two circular vortex ring problems were studied to compare the numerical results with an existing analytic solution of vortex motions and radiated sound. We studied the effects of the aspect ratio for a single elliptic ring and the initial separation distance for two elliptic vortex rings.

4.1. SOUND RADIATION FROM A MUTUAL THREADING OF TWO CIRCULAR VORTEX RINGS

Kambe and Minota [4] calculated the acoustic fields due to the mutual threading and head-on collision of two circular vortex rings analytically by using Dyson's formula for the vortex motion [11]. To verify our numerical method, we calculated the mutual

threading problem of Figure 5(a). Two identical vortex rings were initially chosen, the strength of which was $\Gamma_1 = \Gamma_2 = \Gamma$, the radius of which was $R_1 = R_2 = R_0$, the core radius of which was $c_1 = c_2 = c_0$ and the initial separation of which was $z_1 - z_2 = \Delta z_0$. We compared the analytic results of the velocity of the vortex centroid and the acoustic pressure at far fields for the mutual threading case with our numerical results. The velocity of the vortex centroid U_c, scaled by $U_0 = \Gamma/4\pi R_0$, and the acoustic pressures $\ddot{Q}_{33}$ in equation (5), scaled by $6\Gamma U_0^3$, are shown in Figure 6 for different initial distances of $\Delta z_0/R_0 = 0.3$, 0.5 and 2.0 respectively. The periods of the corresponding $\Delta z_0/R_0$ and $T/(R_0/U_0)$ were 0.130, 0.328 and 3.860 respectively, as analyzed in reference [4]. We could obtain the same values numerically by using parametric blending curves. The initial core radius c_0 was 0.05 for the analytic solution [4]. The corresponding core radius used in the Moore–Rosenhead formula is 0.10542. In the numerical calculations a time step of $\Delta t = 0.001$ with $N = 41$ was used. Generally, jet flows accompanied the vortex pairing motions and generated so-called "vortex pairing noise" [10]. The discrete vortex rings could be generated from the jet flow by acoustically exciting the flow. In reference [10], Bridges and Hussain also pointed out that a primary jet noise source is due to vortex bursting. In addition, it should be noted that the mutual threading phenomena was captured successfully in the laboratory by Yamada and Matsui [16].
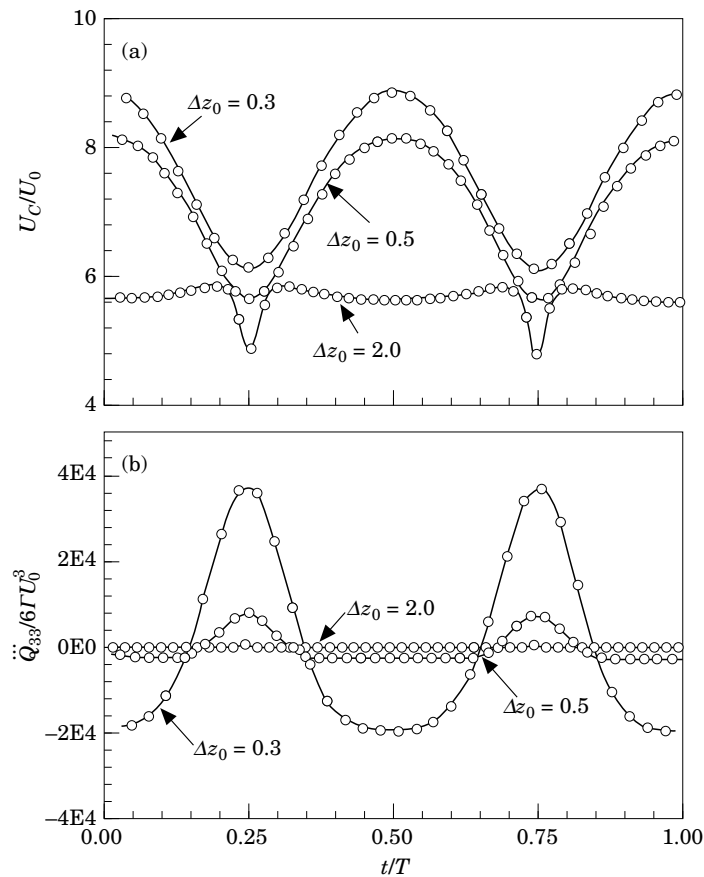

Figure 6. Comparisons of the translational speed and acoustic signals by mutual threading motion. (a) The centroid velocity of two circular vortex rings; (b) acoustic signals. Δz_0 is the initial separation between the two vortex rings ($U_0 = \Gamma/4\pi R_0$). ——, Analytic; ◯, present.

TABLE 1

The parameters of the elliptic rings for fixed major axis length ($a = 1$)

b/a	a	b	Area	c_0	T
0·2	1·0	0·2	0·6283	0·1072	—
0·4	1·0	0·4	1·2566	0·2055	0·52
0·6	1·0	0·6	1·8850	0·2855	0·72
0·8	1·0	0·8	2·5133	0·3468	0·92
1·0	1·0	1·0	3·1416	0·3925	—

4.2. SOUND RADIATION FROM THE EVOLUTION OF AN ELLIPTIC VORTEX RING

A schematic view of the evolution of a single elliptic vortex ring is shown in Figure 5(b). First, we compared our numerical results of the elliptic vortex ring motions with those of Dhanak and De Bernardinis for different aspect ratios [7]. For all the cases, the major axis length was taken as $a = 1·0$ for the comparisons (see Table 1). We selected the same aspect ratios (minor to major axis ratios) as in the reference [7]. In Figures 7, 8 and 9, the evolution processes of the vortex rings for the case of aspect ratios 0·8, 0·6 and 0·2 respectively are described in detail. One can clearly find that the axes are switched from the x_1–x_2 plane views. In Figure 10 are shown the velocities of the vorticity centroid, U_c, for four aspect ratios (0·8, 0·6, 0·4 and 0·2). The numerical results were compared with those of Dhanak and De Bernardinis, and show good agreement. Dhanak and De Bernardinis used $N = 161$ numerical points along the filament for all four cases. We used just $N = 41$ numerical points initially. During the evolution, four additional points were inserted because of local stretching for the case of $b/a = 0·2$. As mentioned previously, additional numerical points are inserted at each time step if the length of a segment is larger than twice the initial length. This numerical insertion compensates for the lack of numerical points internally. As shown in Figure 10, we obtained the same results with a quarter of the numerical points used by Dhanak and De Bernardinis. In the calculations, all of the time steps were taken as $\Delta t = 0·001$. In the cases of the aspect ratios $b/a = 0·8$ and 0·6, as shown in Figures 7, 8 and 10, there exists a periodic tendency in the kinematic motion. For the case of $b/a = 0·2$, however, the periodic tendency disappears, as shown in Figure 10. Dhanak and De Bernardinis used $\Delta t = 0·0001$ for the case of $b/a = 0·2$ but we
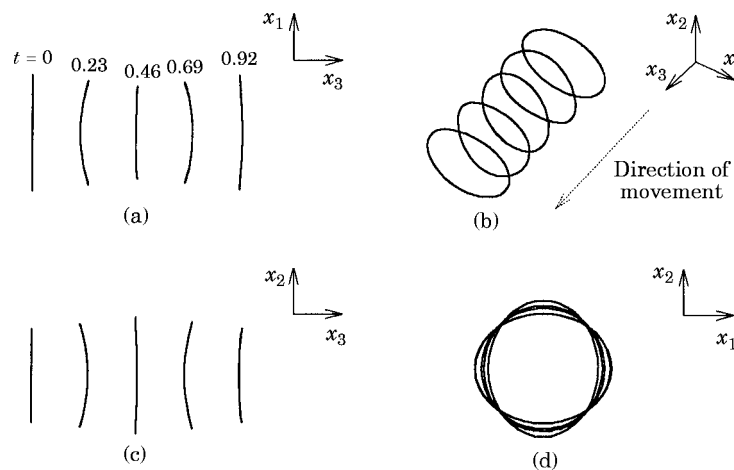

Figure 7. The evolution of a single elliptic vortex ring of $b/a = 0·8$ ($a = 1$). (a) The x_1–x_3 plane; (b) a bird's eye view; (c) the x_2–x_3 plane; (d) the x_1–x_2 plane.
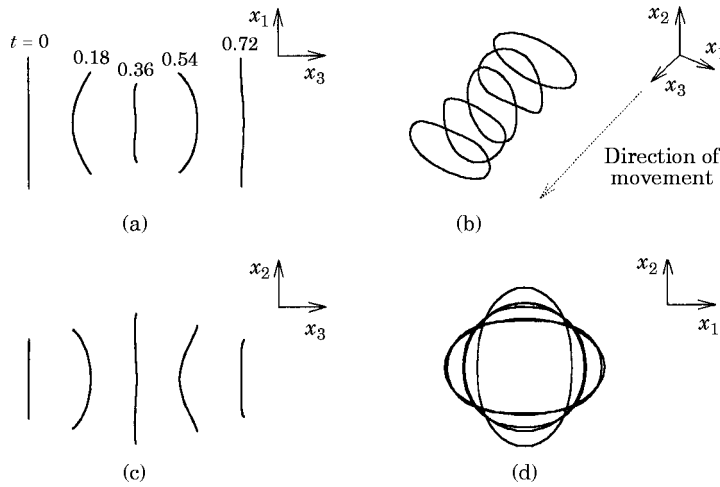
Figure 8. The evolution of a single elliptic vortex ring of $b/a = 0·6$ ($a = 1$). (a) The x_1–x_3 plane; (b) a bird's eye view; (c) the x_2–x_3 plane; (d) the x_1–x_2 plane.

obtained the same result with $\Delta t = 0·001$. We understand that the parabolic blending curve produces a more stable solution than the other interpolation for the time stepping. Especially in the case of $b/a = 0·2$, the filament cores came close to touching each other. It is generally known that touching regions have the vorticity of opposite signs. Viscous diffusion would annihilate the vorticity locally in that region. These results would connect on either side of the region of contact to form two smaller vortex rings. We stopped our calculation at that point.

Second, we calculated the acoustic signals from the evolution of elliptic vortex rings. For all of the sound calculations, a normalized sectional area, that is, the same impulse, was used for comparisons of the acoustic pressures between the different aspect ratios of the elliptic vortex rings (see Table 2). The normalized parameters for all of the aspect ratios are shown in Table 2. The sounds were radiated in the x_1, x_2 and x_3 directions due to the three-dimensional motions of the vortex filaments. We employed the numerical parameters
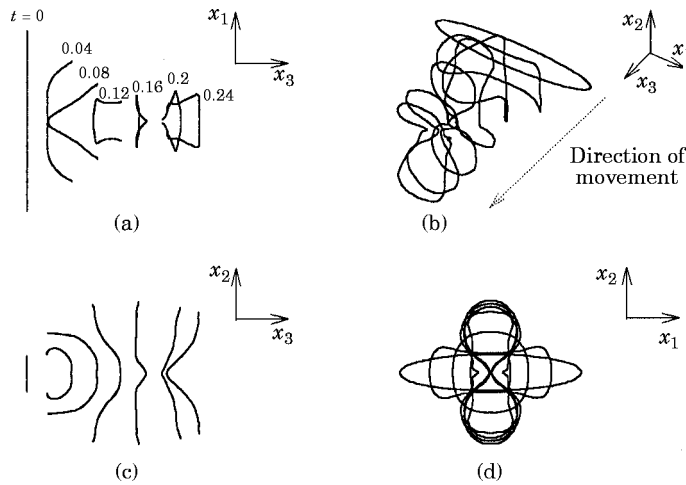

Figure 9. The evolution of a single elliptic vortex ring of $b/a = 0·2$ ($a = 1$). (a) The x_1–x_3 plane; (b) a bird's eye view; (c) the x_2–x_3 plane; (d) the x_1–x_2 plane.
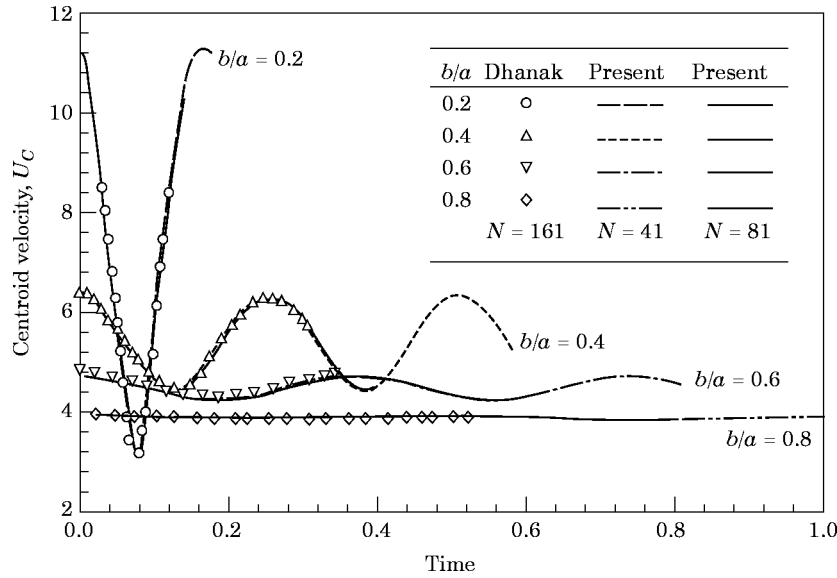
Figure 10. A plot of the centroid velocity versus time for an elliptic vortex ring ($\Delta t = 0{\cdot}0001$ when the axis ratio is $0{\cdot}2$, while other axis ratios have $\Delta t = 0{\cdot}001$; $a = 1$).

$N = 81$ and $\Delta t = 0{\cdot}001$ to calculate the acoustic fields from a single elliptic vortex ring. In general, a coarse time step or the number of numerical points can lead to numerical instability and significant error in the calculation of the sound field. However, the results using the parabolic blending curve show that they are insensitive to the parameters. Figure 11 is shown the acoustic signal $\ddot{Q}_{33}$ for the case of $b/a = 0{\cdot}6$ with various numerical time steps and numerical points. In Figure 11(a) is shown the effect of the time steps ($\Delta t = 0{\cdot}01, 0{\cdot}001, 0{\cdot}0001$) with $N = 81$, and in Figure 11(b) is shown the effect of the numerical points ($N = 41, 81, 161$) with $\Delta t = 0{\cdot}001$. We found that $N = 81$ and $\Delta t = 0{\cdot}001$ was sufficient to calculate the elliptic vortex ring of $b/a = 0{\cdot}6$. The periodic sound pressures of the aspect ratios of $b/a = 0{\cdot}8$ and $0{\cdot}6$ are plotted in terms of $\ddot{Q}_{ii}$ in Figures 12 and 13 respectively. The periods of the elliptic vortex rings (see Table 2) were obtained from the calculated kinematic motion in Figure 10. The major and minor axes were switched at about half the period time, as indicated in the $\ddot{Q}_{11}$ and $\ddot{Q}_{22}$ signals, whereas the period of $\ddot{Q}_{33}$ was the same as that of the vortex motion. For the case of $0{\cdot}8$ as shown in Figure 12, and the amplitude in the direction of the major and minor axes, $\ddot{Q}_{11}$ and $\ddot{Q}_{22}$, were almost the same. The signals of the aspect ratio of $0{\cdot}6$, as shown in Figure 13, became aperiodic and the amplitudes became large as the aspect ratio of the ellipse decreased. This indicates that the acoustic signals are sensitive to the vortex kinematic motion. It is well known that the kinematic motion is aperiodic below an aspect ratio of $0{\cdot}6$ [7]. For the case of $b/a = 0{\cdot}2$, the kinematic motion of the elliptic vortex ring is very complex and the

TABLE 2

The parameters of the elliptic rings for the equivalent enclosing area

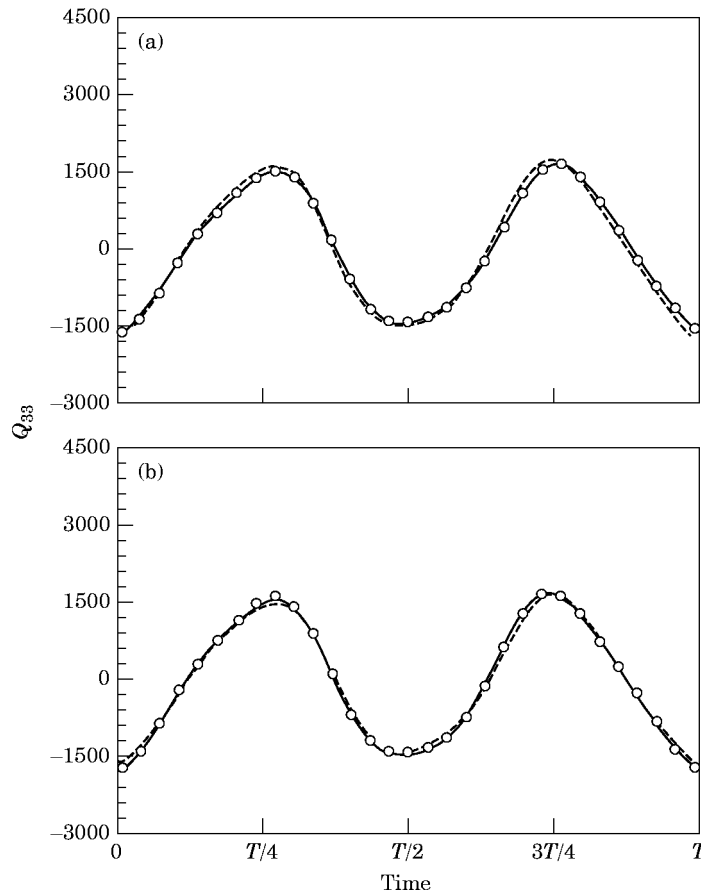| b/a	a	b	Area	c_0	T
0·2	2·236	0·447	3·1416	0·2397	—
0·6	1·291	0·775	3·1416	0·3685	1·23
0·8	1·118	0·894	3·1416	0·3877	1·22

Figure 11. Comparisons of the acoustic signals from the single elliptic vortex ring with various numerical parameters ($b/a = 0.6$, $a = 1.292$). (a) Variations of the time step, $N = 81$: – – – –, $\Delta t = 0.01$; –·–O–·–, $\Delta t = 0.001$; ——, $\Delta t = 0.0001$. (b) variations of the numerical points, $\Delta t = 0.001$: – – – –, $N = 41$; –·–O–·–, $N = 81$; ——, $N = 161$.

acoustic pressure of the elliptic vortex ring has a strong time variation, like a strong pulsating signal, as in Figure 14. We have plotted three special kinematic views of the motion at time $t = 0$, 0.4 and 0.75 in Figure 15. At time $t = 0.4$, the first axis switching phenomena was initiated (see Figures 14 and 15. At that instant, the acoustic signal had a peak in $\ddot{Q}_{22}$. At time $t = 0.75$, the acoustic signal also had a peak. This means that the time variation of the kinematic motion has a large variation at that incidence. At time $t = 0.75$, however, the filament cores touched each other, and the results without viscous diffusion have no physical meaning.

In general, no preferential directions of the acoustic radiation were observed except in the case of an aspect ratio of 0.2. However, the amplitude of the acoustic signals in the major axis direction, $\ddot{Q}_{11}$, was larger than that in the minor one, $\ddot{Q}_{22}$, at the beginning.

4.3. SOUND RADIATION FROM TWO ELLIPTIC VORTEX RINGS

For the case of the interaction of two elliptic vortex rings, the directivity pattern of the acoustic signal was similar to that of two circular vortex rings except for the axis switching effect, which resulted initially in complicated vortex motion and acoustic signals. Two elliptic vortex rings, A and B, were placed in the back and fore positions respectively, as
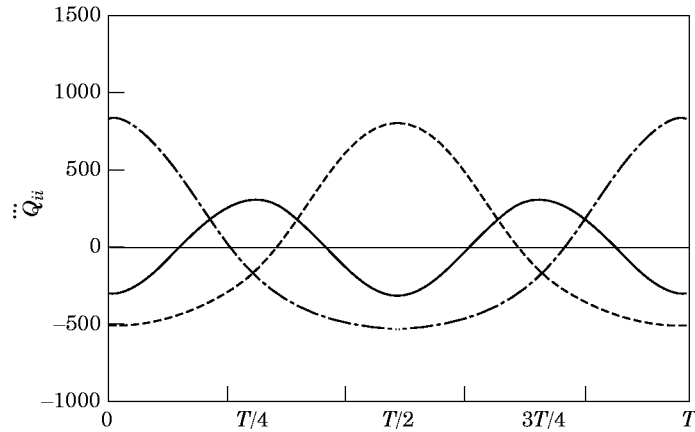
Figure 12. The components of the acoustic signals due to the motion of a single elliptic vortex ring in a period T ($b/a = 0.8$, $a = 1.118$). $-\cdot-\cdot-$, $\dddot{Q}_{11}$; $----$, $\dddot{Q}_{22}$; $-\!\!-\!\!-$, $\dddot{Q}_{33}$.

shown in Figure 5(c). For all of the sound calculations, a normalized sectional area was used for comparisons of the acoustic pressures between different aspect ratios of the elliptic vortex rings (see Table 2). We adopted $N = 81$ as the initial numerical points to calculate the sound radiation from two elliptic vortex rings. These numerical points were sufficient for a normal aspect ratio ($b/a = 0.6$ or 0.8), as verified in Figure 11. During the calculation, we inserted a numerical point when the length of a segment was larger than twice the initial length.

The kinematic motion for the case of $b/a = 0.8$, $N = 81$, $\Delta t = 0.001$ and $\Delta z_0 = 0.5$ is shown in Figure 16. We show typical views at the instant of slip-through motion at $t = 0.08$, 0.24, 0.44 and 0.60. We could obtain periodic pairing motion at every 0.36. For the single elliptic ring case, the axis switching occurred at every 1.22 (see Table 2 and Figure 12). The leap-frogging motion, as it is sometimes called, is the mutual threading motion in the pairing process, where the trailling vortex ring contracts and rushes through the leading vortex that is already enlarged, and this slip-through process is repeated with an exchange of roles. In this case, we found strong periodicity in the kinematic motion and acoustic signals.
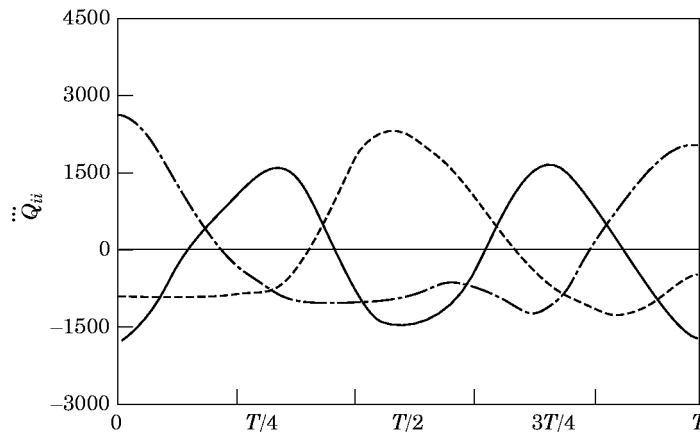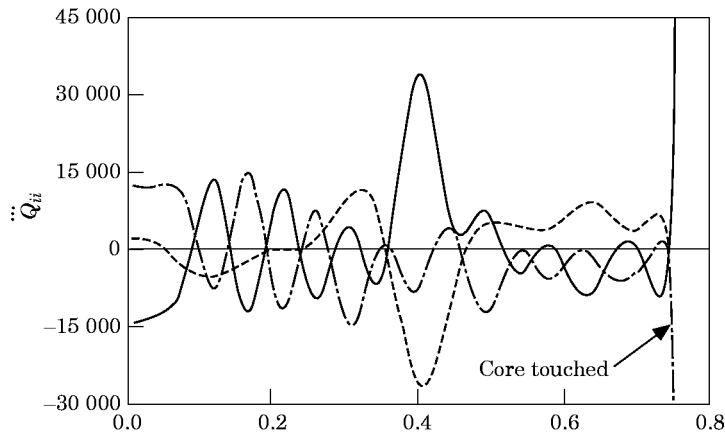
Figure 13 The components of the acoustic signals due to the motion of a single elliptic vortex ring in a period T ($b/a = 0.6$, $a = 1.291$). $-\cdot-\cdot-$, $\dddot{Q}_{11}$; $----$, $\dddot{Q}_{22}$; $-\!\!-\!\!-$, $\dddot{Q}_{33}$.

Figure 14 The components of the acoustic signals due to the motion of a single elliptic vortex ring in a period T ($b/a = 0.2$, $a = 2.236$). $-\cdot-\cdot-$, $\dddot{Q}_{11}$; $----$, $\dddot{Q}_{22}$; ———, $\dddot{Q}_{33}$.

Two elliptic vortex rings had axis switching phenomena with the leap-frogging motion. The periods of both axes switching were nearly half of the leap-frogging motion, as shown in Figure 17. The slip-through motion in Figure 16 occurred at every peak of the centroid velocity, as shown in Figure 17. The first peak was at nearly $t = 0.09$ and the second was at about 0.27, and so forth. The maximum and minimum centroid velocities of the vorticity corresponded to the axes of the inner and outer elliptic vortex rings, respectively. Two slip-through motions occurred at every period. The variation of the x_1- and x_2-axis lengths of the elliptic vortex ring is represented in Figure 18. We can find approximately the axis switching instant when the plane view of two elliptic vortex rings became circular shapes. That is, the lengths of the two axes became the same at $t = 0.22$ and 0.72 for the vortex rings A and B. Those periods are longer than the leap-frogging periods at this initial separation distance. In Figure 19 are shown the signals of each acoustic component for the above case. The instant of the first peak in the $\ddot{Q}_{33}$ signal (corresponding to the moving direction) corresponded approximately to the 1/4 period of the leap-frogging motion (see Figure 7 for two circular vortex rings). We could obtain a period of about 0.36 from that
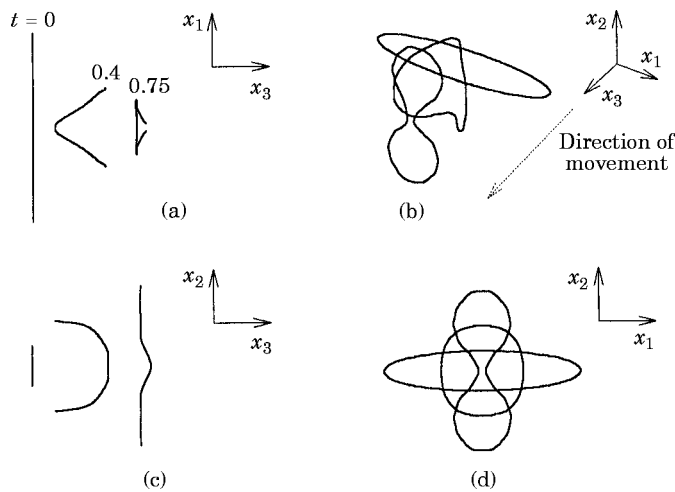

Figure 15. Evolutionary views of three instants of a single elliptic vortex ring ($b/a = 0.2$, $a = 2.236$ at initial instant). (a) The x_1–x_3 plane; (b) a bird's eye view; (c) the x_2–x_3 plane; (d) the x_1–x_2 plane.
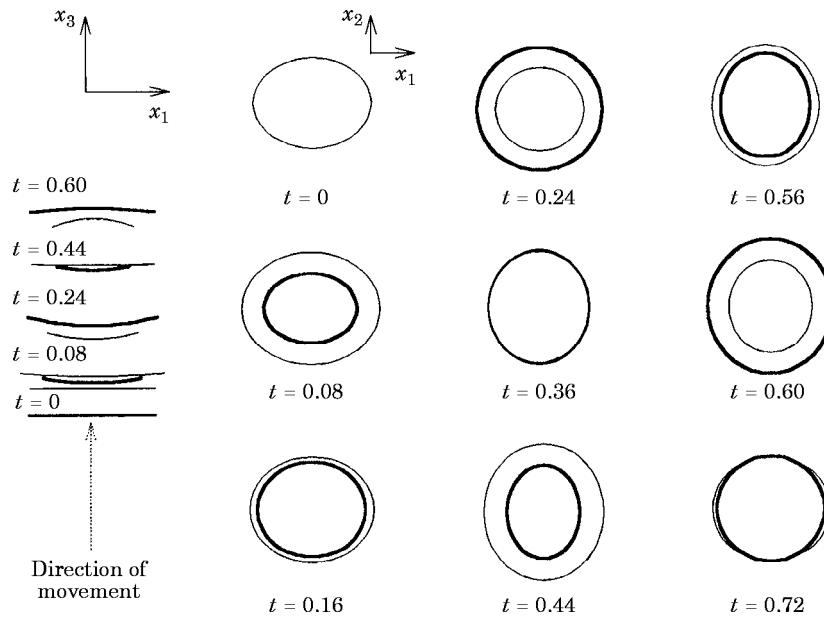
Figure 16. A frontal view of two elliptic vortex rings with pairing motion ($b/a = 0.8$, $\Delta z_0 = 0.5$). The bold line is initially the rearward elliptic vortex ring (ring A).

signal, as shown in Figure 19. From the figure, the peak value of $\ddot{Q}_{22}$ at $t \approx 0.88$ is larger than that of $\ddot{Q}_{11}$ these being related to the minor and major axis directions, respectively, in the first period. In the second period, the peak value of $\ddot{Q}_{11}$ near $t \approx 0.44$ was larger than that of $\ddot{Q}_{22}$. The value of $\ddot{Q}_{11}$ is also related to the minor axis direction, because the axes are interchanged. Therefore, the preferential directions of sound generation were interchanged during several periods. In both experiments for the elliptic [16, 17] or circular jet with the mutual threading experiment [10], leap-frogging phenomena were observed just once or twice, so the first or the second peaks in $\ddot{Q}_{11}$ and $\ddot{Q}_{22}$ would determine the preferential direction of the sound radiation.
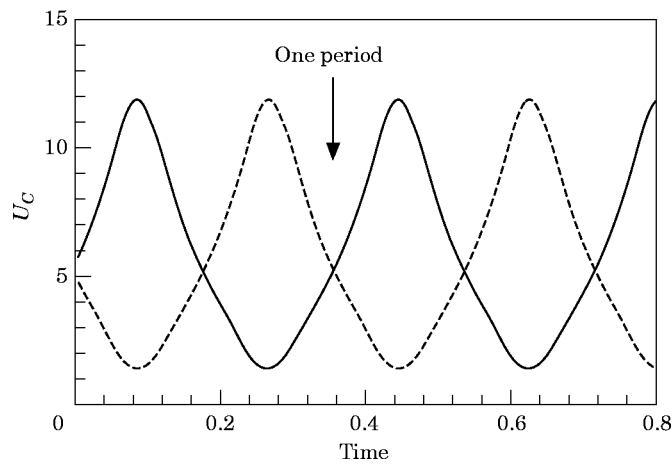

Figure 17. The centroid velocity of two elliptic vortex rings ($b/a = 0.8$, $\Delta z_0 = 0.5$, rings A and B initially the rearward and forward elliptic ring respectively). ——, Ring A; – – – –, ring B.
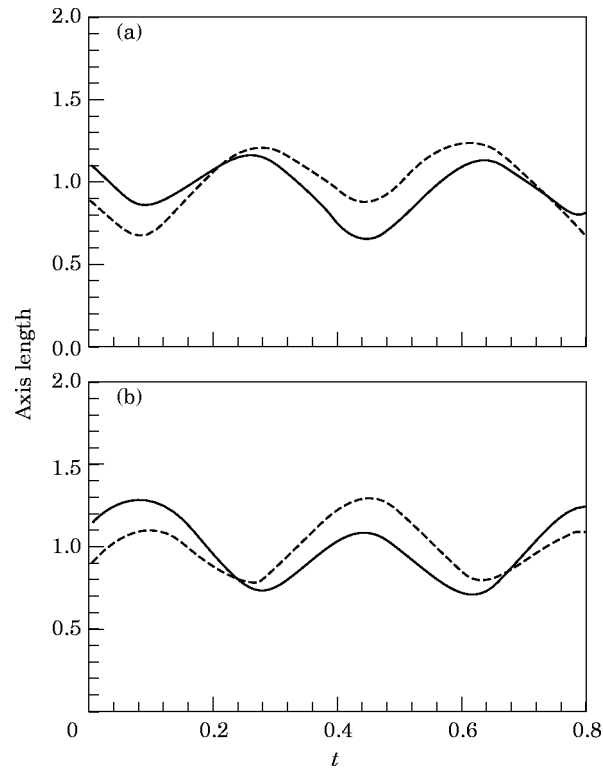
Figure 18. The time variation of the projected axis length for elliptic rings A and B in leap-frogging motion (projected plane, x_1–x_2 plane; $b/a = 0.8$; $\Delta z_0 = 0.5$). (a) Ring A; (b) ring B. ——, x_1-axis; $----$, x_2-axis.

An aspect ratio of 0·6 was chosen to investigate the effect of the separation distance on the vortex motion and the acoustic signal. Three typical initial separation distances were selected: $\Delta z_0 = 0.5$, 0.8 and 2.0, with $N = 81$ and $\Delta t = 0.001$. The calculations were repeated with a time step of $\Delta t = 0.0002$, leading to practically the same curves. In Figure 20 is shown the configuration of the leap-frogging and the axis switching motion of two
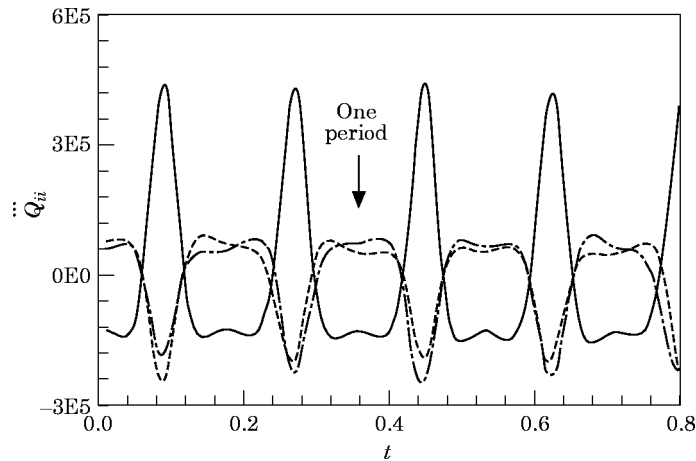

Figure 19. The components of the sound signals due to the motion of two elliptic vortex rings ($b/a = 0.8$, $\Delta z_0 = 0.5$). $-\cdot-\cdot-$, $\dddot{Q}_{11}$; $----$, $\dddot{Q}_{22}$; ——, $\dddot{Q}_{33}$.
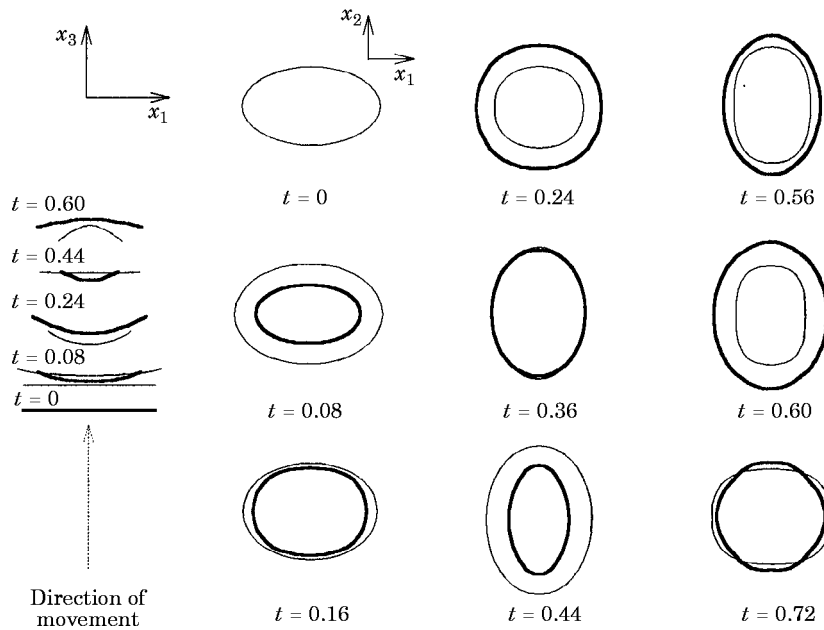
Figure 20. A frontal view of two elliptic vortex rings with leap-frogging motion ($b/a = 0.6$, $\Delta z_0 = 0.5$). The bold line is initially the rearward elliptic vortex ring (ring A).

elliptic vortex rings with an initial separation distance of $\Delta z_0 = 0.5$. The acoustic signals simulate the case of $b/a = 0.6$ and $\Delta z_0 = 0.5$, as shown in Figure 21, with a numerical time step of $\Delta t = 0.001$. One can compare the kinematic motion and acoustic signals for the above case with those of $b/a = 0.8$ and $\Delta z_0 = 0.5$. The difference is that the periodic motions and acoustic signals of $b/a = 0.6$ have deteriorated after the second slip-through motion.

The results when the initial separation instance $\Delta z_0 = 0.8$ with $b/a = 0.6$, $N = 81$ and $\Delta t = 0.001$, are represented in Figures 22 and 23. In Figure 22, we found two slip-through motions at about $t = 0.21$ and $t = 0.66$. The two vortex rings are highly distorted at
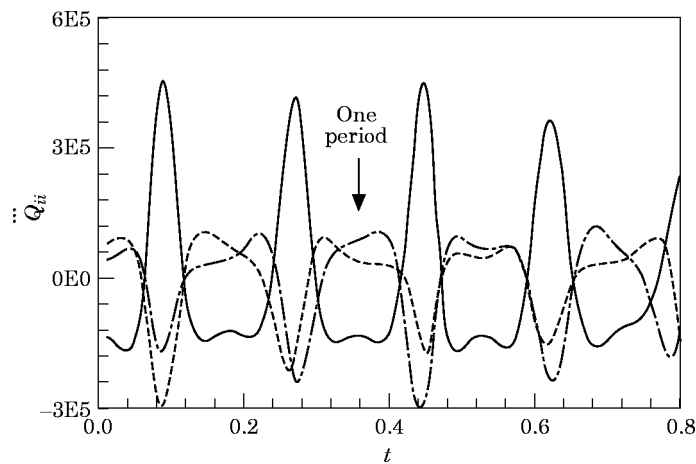

Figure 21. The components of the sound signals due to the motion of two elliptic vortex ring, ($b/a = 0.6$, $\Delta z_0 = 0.5$). $-\cdot-\cdot-$, $\dddot{Q}_{11}$; $----$, $\dddot{Q}_{22}$; $\longrightarrow$, $\dddot{Q}_{33}$.
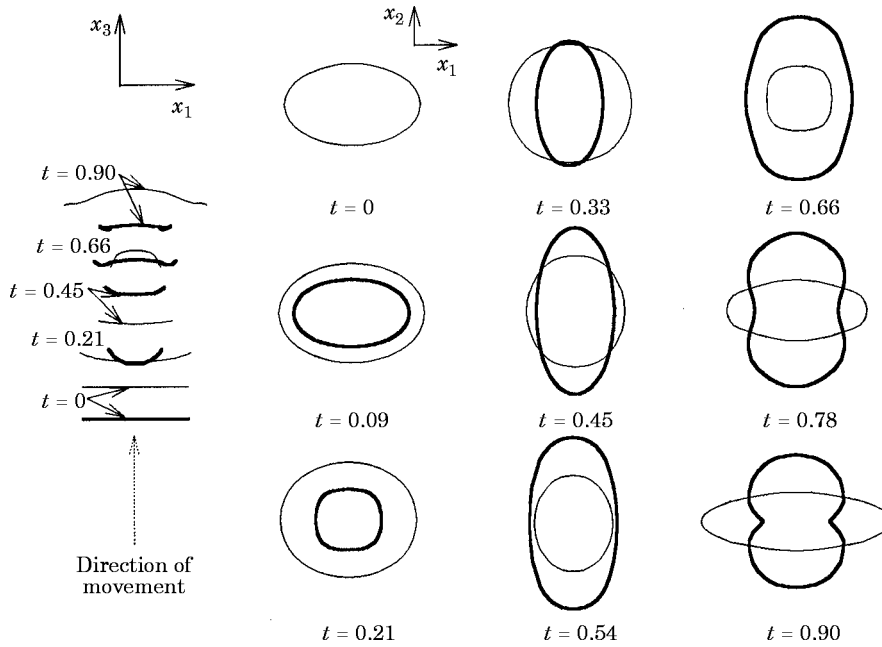
Figure 22. A frontal view of two elliptic vortex rings with leap-frogging motion ($b/a = 0.6$, $\Delta z_0 = 0.8$). The bold line is initially the rearward elliptic vortex ring (ring A).

$t = 0.9$, especially ring A. In Figure 23, there are two acoustic peaks which are related to the two slip-through motions. That for $\ddot{Q}_{22}$ is larger than that for $\ddot{Q}_{11}$ at the instant of the first peak. However, the roles are reversed at the instant of the second peak. For the second slip-through motion at about $t = 0.66$, the acoustic signals have sinusoidal peaks, which have a different tendency from the first slip-through instant. Before the slip-through motion, the minor axis directions of the two vortex rings are the same (see the shape at $t = 0.54$ in Figure 22). After the second slip-through motion at $t = 0.78$, however, the shape of ring A is changed into a shape like a cocoon, while the shape of ring B is changed to the original elliptic shape. The time variation of the shape of vortex ring A significantly
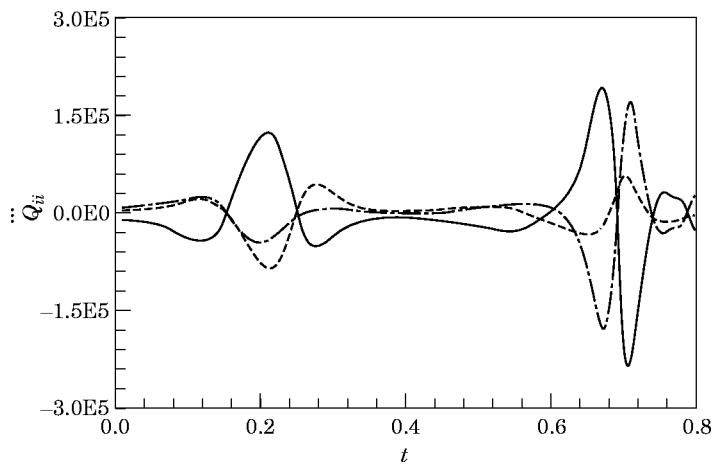

Figure 23. The components of the sound signals due to the motion of two elliptic vortex ring, ($b/a = 0.6$, $\Delta z_0 = 0.8$). $-\cdot-\cdot-$, $\ddot{Q}_{11}$; $----$, $\ddot{Q}_{22}$; $\underline{\quad\quad}$, $\ddot{Q}_{33}$.
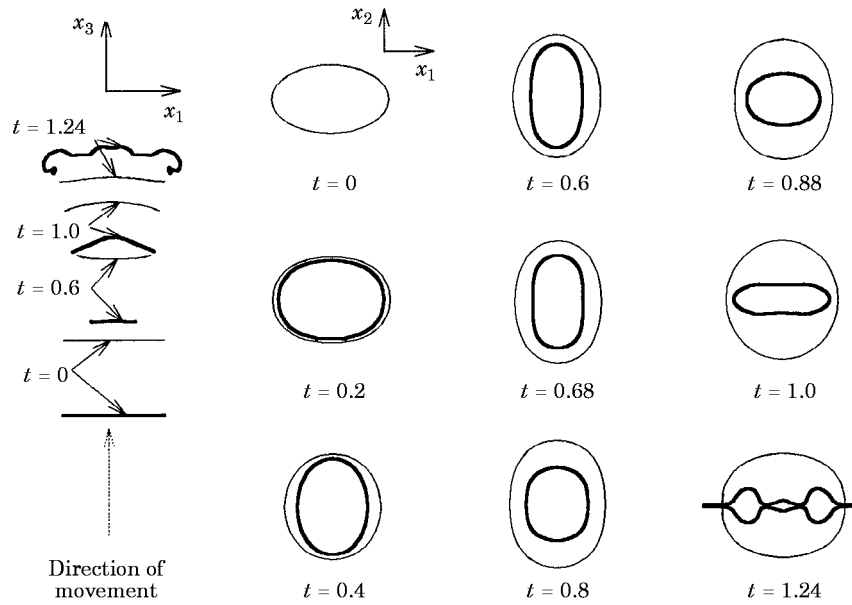
Figure 24. A frontal view of two elliptic vortex rings with leap-frogging motion ($b/a = 0.6$, $\Delta z_0 = 2.0$). The bold line is initially the rearward elliptic vortex ring (ring A).

affects the acoustic signal of $\ddot{Q}_{11}$ in the x_1 direction, the amplitude of which is comparable to the $\ddot{Q}_{33}$ signals, as shown in Figure 23.

In Figure 24, we used the same value of $b/a = 0.6$ and an initial separation distance of $\Delta z_0 = 2.0$ with $N = 81$ and $\Delta t = 0.001$. We found that the switching of the two axes occurred for vortex ring A at about $t = 0.4$ and 0.88. The period of the axis switching for vortex ring A is smaller than ring B, as shown in Figure 24. At $t = 1.0$, one side of ring A is very close to ring B. At that point, a high induced velocity makes that portion of the filament rake shaped, and the other portion of ring A rushes out at high velocity. For these reasons, the vortex filament of elliptic vortex ring A is highly deformed at $t = 1.24$. When the initial separation distance is larger than 2.0, switching phenomena involving more than two axes will occur before the first leap-frogging motion. The period of the axis switching is comparable to that of a single elliptic vortex ring ($T = 1.23$). Then the axis switching phenomena are expected to be a dominant process and will influence the periodicity of the acoustic signals. Therefore, the dominant acoustic direction due to the pairing depends on the initial gap distance. The acoustic signal is shown in Figure 25. Before the slip-through motion, the acoustic signals have a similar trend to the single elliptic vortex ring, as shown in Figure 13. The acoustic signals of $\ddot{Q}_{11}$ and $\ddot{Q}_{22}$ seem to become aperiodic because of the pairing frequency for the system in addition to the axis switching frequencies. At the instant of slip-through motion at $t = 1.12$, the signal has a large acoustic peak, as shown in Figure 25. Generally, the two frequencies are not the same. The frequencies influencing the kinematic motions of the vortex rings and also the acoustic signals are dependent on the aspect ratios of the elliptic vortex rings and the initial separation distances of the two elliptic vortex rings.

5. CONCLUSIONS

In this study, we have obtained kinematic motions and acoustic fields numerically for elliptic vortex rings, the motions of which are three-dimensional. For a single circular
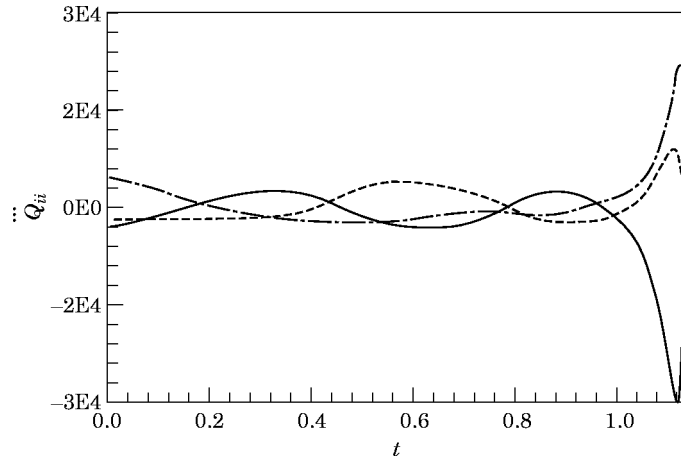
Figure 25. The components of the sound signals due to the motion of two elliptic vortex rings, $(b/a = 0\cdot6, \Delta z_0 = 2\cdot0)$. $-\cdot-\cdot-$, $\dddot{Q}_{11}$; $----$, $\dddot{Q}_{22}$; $-\!\!-\!\!-$, $\dddot{Q}_{33}$.

vortex ring, the far field acoustic pressures have been compared with the analytic results, and show a high level of agreement. For the case of a single elliptic vortex ring, the evolution processes generated acoustic pressure fluctuations which were different from those of a single circular ring. This difference is due to the axis switching motion of the elliptic vortex ring, which has periodic pressure fluctuations for a moderate aspect ratio of the minor and major axes. For the case of the two elliptic vortex ring pair, stronger acoustic pressures were radiated in the minor axis direction than in the major one because of the first leap-frogging motion, in addition to the pressure in the convection direction. The axis switching phenomenon is also accompanied by the leap-frogging motion. Therefore, three dominant eigenfrequencies exist: the first and the second from the axis switching phenomena of each elliptic ring, and the third from the leap-frogging; that is, the pairing phenomenon. These acoustic phenomena could be obtained by accurately determining the vortex motions. The motions were calculated by interpolating the discretized vortex filament with parabolic blending curves. The distorted curves were redistributed at each time step to improve the resolution of the vortex filaments. The motions and acoustic signals for the elliptic vortex rings are strongly dependent on the aspect ratios of the minor to major axis lengths and the initial separation distances between the two elliptic vortex rings.

REFERENCES

1. A. POWELL 1964 *Journal of the Acoustical Society of America* **36**, 177–195. Theory of vortex sound.
2. M. S. HOWE 1975 *Journal of Fluid Mechanics* **71**, 625–673. Contribution of the theory of aerodynamic sound, with application to excess jet noise and the theory of the flute.
3. W. MÖHRING 1978 *Journal of Fluid Mechanics* **85**, 685–691. On vortex sound at low Mach number.
4. T. KAMBE and T. MINOTA 1981 *Journal of Sound and Vibration* **74**, 61–72. Sound radiation from vortex systems.
5. D. G. CRIGHTON 1981 *Journal of Fluid Mechanics* **106**, 261–298. Acoustics as a branch of fluid mechanics.
6. R. J. ARMS and F. R. HAMA 1965 *Physics of Fluids* **8**, 553–559. Localized-induction concept on a curved vortex and motion of an elliptic vortex ring.

7. M. R. DHANAK and B. DE BERNARDINIS 1981 *Journal of Fluid Mechanics* **109**, 189–216. The evolution of an elliptic vortex ring.
8. D. W. MOORE 1972 *Aeronautical Quarterly* **23**, 307–314. Finite amplitude waves on aircraft trailing vortices.
9. W. MÖHRING 1990 *Journal of Sound and Vibration* **140**, 155–162. Sound radiation by two elliptic vortex rings.
10. J. E. BRIDGES and A. K. M. F. HUSSAIN 1978 *Journal of Sound and Vibration* **117**, 289–311. Roles of initial condition and vortex pairing in jet noise.
11. F. W. DYSON 1893 *Philosophical Transactions of the Royal Society of London* **A184**, 1041–1101. The potential of an anchor ring, part II.
12. S. K. TANG and N. W. M. KO 1993 *Journal of Fluids Engineering* **115**, 425–435. A study on the noise generation mechanism in a circular air jet.
13. M. J. LIGHTHILL 1952 *Proceedings of the Royal Society of London* **A211**, 564–587. On sound generated aerodynamically, I: general theory.
14. P. G. SAFFMAN 1970 *Studies in Applied Mathematics* **49**, 371–380. The velocity of viscous vortex rings.
15. D. F. ROGERS 1990 *Mathematical Elements for Computer Graphics*. New York: McGraw-Hill.
16. H. YAMADA and T. MATSUI 1978 *Physics of Fluids* **21**, 292–294. Preliminary study of mutual slip-through of a pair of vortices
17. H. S. HUSAIN and A. K. M. F. HUSSAIN 1991 *Journal of Fluid Mechanics* **233**, 439–482. Elliptic jets, part 2: dynamics of coherent structures: pairing.